

## ORIGINAL RESEARCH PAPER

# Matrix pencil method for topography-adaptive digital beam-forming in synthetic aperture radar

Tobias Rommel<sup>1</sup>  | Sigurd Huber<sup>1</sup>  | Marwan Younis<sup>1</sup>  | Madhu Chandra<sup>2</sup>
<sup>1</sup>German Aerospace Center (DLR), Microwaves and Radar Institute, Wessling, Germany

<sup>2</sup>Professorship of Microwave Engineering and Electromagnetic Theory, Technical University Chemnitz, Chemnitz, Germany

## Correspondence

Tobias Rommel, German Aerospace Center (DLR), Microwaves and Radar Institute, Muenchener Strasse 20, 82234 Wessling, Germany.  
Email: [tobias.rommel@dlr.de](mailto:tobias.rommel@dlr.de)

## Abstract

Spaceborne synthetic aperture radar (SAR) with digital beam-forming (DBF) in elevation uses very sharp time-variant antenna beams to improve the signal-to-noise ratio (SNR) and range ambiguity-to-signal ratio. In acquisition scenarios of imprecisely known Earth topography, however, antenna pointing might be mismatched with surface geometry. To handle this issue, it is suggested that preprocessing is applied to DBF to determine the angle of the incident echo signal on the planar antenna array. The authors derive a method that estimates the direction of arrival on the acquired raw data with high accuracy in real time. The method is based on the matrix pencil, which is a common approach in mathematics for solving linear equation systems. As a key innovation, this paper describes further improvements and adaptations to SAR scenarios and provides a possible concept for practical implementation. For proof of concept, a series of different simulation tasks is performed.

## 1 | INTRODUCTION

Since the development of the first synthetic aperture radar (SAR) in 1951, radar has become an essential sensor for imaging applications. Manifold fields of application ranging from climate change research to change detection, and 4-D mapping to earthquake and flood monitoring, are covered by SAR. Due to the high demand for global SAR data sets, state-of-the-art sensors have reached their limits in resolution, swath width, repeat cycle, and flexibility. To solve SAR-inherent limitations, a new generation of SAR sensors with multiple transmit and receive channels (MIMO) and digital beam-forming (DBF) capabilities is proposed in several studies [1–3]. However, such DBF-SAR techniques require an antenna with a narrow half-power beamwidth (*HPBW*). In the presence of unknown Earth topography, when the assumed geometrical model of the Earth's surface is complex, antenna pointing might be mismatched with surface geometry. Depending on the antenna *HPBW* and the error in the assumed Earth model, the resulting mispointing might lead to a significant loss of gain. To handle this issue, in principle, existing digital elevation model (DEM) data can be uploaded to the satellite and used for

correction. But the amount of data for a global DEM upload might be too large, and there might be areas with outdated height profiles (e.g. due to earthquakes and volcanic eruptions). As an alternative solution, in [4], it was suggested that an additional algorithm should be applied prior to DBF to estimate, from the acquired raw data, the angle of the incident echo signal on the planar antenna array for a certain recorded echo window (i.e. receive interval *PRI*). This angle is also known as the angle of arrival (AoA). Thereupon, the DBF steering vector can be adapted to form an antenna beam that points in the correct direction.

Because the relation between antenna beam pattern and radiated/impinging signal is usually described using spectral frequency components [5], it is valid to transfer that task to common spectral estimation algorithms [6]. These spectral estimators are used to obtain the distribution of the signal power over frequency for sampled signals in the time domain. Due to the strong correspondence between the *spatially dependent* frequency and *temporal* signal frequency, many spectral estimators can be used for AoA estimation. In the meantime, more than 20 different spectral estimation algorithms have been derived [6]. They can be categorized into two

classes: non-parametric and parametric methods. Non-parametric estimators evaluate the power spectral density (PSD) of the input signal by direct and linear analysis of the whole spectrum. Parametric estimators are also known as model-based estimators, as they are based on an assumed signal model. This model parametrizes the spectrum of known structures, and the used PSD estimator determines the value of the desired parameter. Since parametric estimators use additional information, they lead to more accurate results (if the signal model is correct). SAR is based on a signal model, and information about the signal structure and some properties about the geometric relations between SAR and Earth are known. Therefore, the preferred class of high-resolution parametric estimators can be applied. Established parametric algorithms are spectral Multiple Signal Classification (MUSIC) [7], root MUSIC [8], and Estimation of Signal Parameters using Rotational Invariance Techniques (ESPRIT) [9]. These estimators are computationally very intensive because they need to compute a correlation matrix from the received raw data. In addition, such estimators are derived for more common problems in communication and hence are not very effective for SAR.

To fulfil the highest quality standards in DBF-SAR and MIMO-SAR, it is necessary to derive an effective application-orientated algorithm to avoid the previously mentioned mispointing effect. It has been found that the matrix pencil (MP) method, which was originally intended to solve a linear equation system, serves as a good starting point [10, 11]. In the meantime, the MP also finds application in some basic angular estimation problems [12, 13] and even for back projection processing of inverse SAR [14]. This parametric approach does not need a calculation of a covariance matrix. Regarding run time, this is a significant advantage in contrast to other established methods, such as spectral MUSIC, Root MUSIC, or ESPRIT (a comparison of the run time between the estimators is given in Section 4.1). SAR is an imaging sensor and evaluates the signal within an enormous interval of incidence angles of typically more than  $20^\circ$ . This leads to a challenge if the AoA estimator delivers only certain angles. Thus, the side-looking sensor geometry is exploited here, and the time-variant AoA is divided into individual cells. Via sliding time windows and adapted averaging methods, the underlying task is transferred to a point target-like situation so that the adjusted AoA estimator will work. Finally, the individual estimates are combined and form the basis for topography-adaptive DBF. Because the MP method shall also be applied on-board, a concept for a possible practical implementation is given, which enables a precise and stable topography-adaptive elevation DBF in real-time.

The paper is structured as follows. In the beginning, the detailed problem formulation and error analysis in the case of a mismatch between the theoretical topographic model used for the DBF algorithm and reality is given. After introducing the signal model, the MP in its basic form is derived. Then further improvements on the MP and problem-based adaptations to DBF-SAR are derived. The second section ends with a concept

for a practical implementation on-board in real-time. To gain an impression of the suggested algorithm's behaviour, capabilities, and performance, the paper concludes with simulation results.

## 2 | ANTENNA MISPOINTING FOR UNKNOWN TOPOGRAPHY

For many future spaceborne DBF-SAR, the SCORE technique (SCan On REceive) is proposed [15]. There, a narrow, time-variant elevation antenna beam follows the echo signal on the ground. This leads to an increased *SNR* and a strongly reduced range ambiguity-to-signal ratio. But in most publications about SCORE and DBF-SAR, it is assumed that the geometric relation between radar sensor and the Earth is known, and the time-variant receive antenna beam tracks SAR echoes according to the underlying geometric model. However, for an unknown topography, this relation is not established. This has been pointed out especially in [16, 17]. Therein the authors denote this effect as SCORE pattern loss. Figure 1 illustrates this distortion for a constant slant range distance  $r_0$  at mountains of height  $\Delta h$ .

Under the assumption of a spaceborne scenario with spherical geometry, Figure 2 shows a plot of the antenna mispointing with an orbit height of  $h = 600$  km for the steering angles  $15^\circ$ ,  $20^\circ$ ,  $30^\circ$ , and  $42^\circ$ . As can be seen, the antenna mispointing increases almost linearly with increasing topographic height. At relatively flat areas with vertical terrain differences of less than 1.5 km, the echo may impinge at the receive antenna with an angular offset of around  $0.2^\circ$ – $0.5^\circ$ . Comparing this value with an antenna *HPBW* of  $0.4^\circ$ , in the worst-case scenario, not only is there a significant loss of gain but also, the antenna might point in a completely different direction.

## 3 | MATRIX PENCIL METHOD

In the first part of this section, we will derive the MP algorithm in its basic form to estimate the AoA profile along elevation. Afterwards, extensions using averaging techniques are given to enhance the probability of correct estimates. Additional improvements to address inherent SAR effects on the received signal and a concept for practical implementation on-board are also presented.

### 3.1 | Signal model for direction of arrival estimation

Like other established AoA estimation methods, such as MUSIC [7], Root MUSIC [8], and ESPRIT [9], the MP is also based on a point target model with multiple distinct targets. It is important to note that any deviations due to extended pulses (cf. [18]), interfering signals (e.g., MIMO), or extended surface

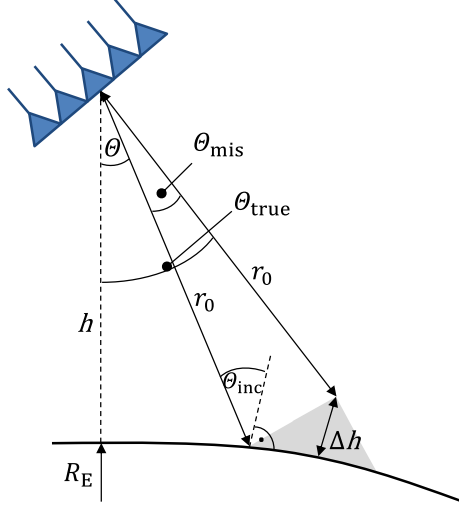


**FIGURE 1** Illustration of the antenna mispointing due to topographic changes

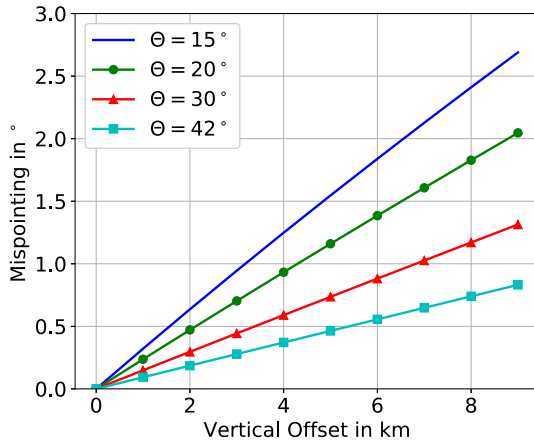


**FIGURE 2** Antenna mispointing for various terrain heights and steering angles

scatterers, result in errors during the calculations and affect the accuracy and stability of the algorithm. For ease of understanding, we firstly derive the simplified point target signal model<sup>1</sup>. Estimation errors for more complex scenarios are analysed at the end of this paper via simulations.

Signal processing and hence also the AoA estimation is done at the digital stage of the radar receiver. Thus, it is worthwhile to directly write the receive signal in its down-converted and discretized form:

$$\mathbf{u}[p] = \mathbf{A}[p] \cdot \sigma \cdot s[p - p_0] + \mathbf{n}[p], \quad (1)$$

while  $p$  is the discrete index of the time sample ( $p \in \mathbb{N}_0^+$ ) and  $\sigma$  is the column vector of individual backscatter amplitudes (size:

$N_{\text{Tar}}$ ).  $s$  is the transmit waveform (e.g. chirp),  $p_0$  is the index of the round-trip time-delay from the transmit antenna to the target and back to the first receive antenna element, and  $\mathbf{n}$  is Additive White Gaussian Noise.  $\mathbf{A}$  is the antenna steering matrix:

$$\mathbf{A} = [\mathbf{a}_0, \mathbf{a}_1, \dots, \mathbf{a}_{N_{\text{Tar}}-1}], \quad (2)$$

of the dimensions  $N_{\text{Rx}} \times N_{\text{Tar}}$  (no. of receive channels  $\times$  no. of point targets) and  $\mathbf{a}_m$  are the steering vectors for the  $m^{\text{th}}$  target of the linear antenna array with equispaced elements:

$$\mathbf{a}_m = [z_m^0, z_m^1, \dots, z_m^{N_{\text{Rx}}-1}]^T, \quad (3)$$

with  $^T$  being the transpose of the vector and

$$z_m[p] = \exp(j \cdot \Delta\varphi_m[p]) = \exp\left(j \cdot \frac{2\pi}{\lambda} \cdot d \cdot \sin(\vartheta_m[p])\right). \quad (4)$$

$j$  is the complex constant,  $\Delta\varphi_m$  is the phase shift of the receive signal between two adjacent receive channels of separation  $d$ ,  $\vartheta_m$  is the respective AoA w.r.t. boresight of the antenna array, and  $\lambda$  is the centre wavelength of the RF echo signal. It is important to note that the exponential terms lead only to a relative phase shift between the elements of  $\mathbf{u}$  and do not distort the amplitudes. If all possible values of  $z_m$  are drawn on the complex plane, the values lie exactly on the unit circle. However, additional noise contributions cause distortions, which adversely affect these positions. In the next section, we concentrate on the undistorted case, and afterwards we introduce advanced processing methods to improve the estimator's accuracy and stability in presence of noise and other interference.

### 3.2 | Angle of arrival estimation via the matrix pencil

An MP in mathematics is a linear equation system consisting of matrices with complex elements [10, 11]. The equations can be solved by finding the generalized eigenvalues of the MP. This standard task in mathematics was adapted to angular estimation problems in electrical engineering. The first derivations can be found in [12, 13].

To form the MP, at first the received raw data signals (cf. Equation 1) at a certain instant of time  $p$  and receive antenna element are arranged into a matrix of form

$$\mathbf{Y}[p] = \begin{bmatrix} u_0[p] & u_1[p] & \cdots & u_L[p] \\ u_1[p] & u_2[p] & \cdots & u_{L+1}[p] \\ \vdots & \vdots & \ddots & \vdots \\ u_{N_{\text{Rx}}-L-1}[p] & u_{N_{\text{Rx}}-L}[p] & \cdots & u_{N_{\text{Rx}}-1}[p] \end{bmatrix}. \quad (5)$$

<sup>1</sup>Any influences by the antenna element pattern and mutual coupling are neglected for ease.

a matrix with this symmetric arrangement is also called Hankel matrix. The pencil parameter  $L$  determines its shape and must satisfy the conditions.

$$N_{\text{Tar}} \leq L \leq N_{\text{Rx}} - L \quad \text{if } N_{\text{Rx}} \text{ is even,} \quad (6)$$

$$N_{\text{Tar}} \leq L \leq N_{\text{Rx}} - L + 1 \quad \text{if } N_{\text{Rx}} \text{ is odd.} \quad (7)$$

In principle,  $L$  can be arbitrarily chosen within these intervals. As  $L$  determines the amount of overlap between the two formed antenna subarrays, its value affects the accuracy of the estimated angle. In dependence on the noise level of the received signal, we recommend choosing  $L$  within the interval  $N_{\text{Rx}}/3 \leq L < N_{\text{Rx}}/2$  for either more efficient noise suppression or improved resolution if the number of AoAs is not known beforehand.

At this point, already one important limitation of the MP method becomes noticeable. To estimate a total number of  $N_{\text{Tar}}$  angles, at least  $2N_{\text{Tar}}$  antenna elements are necessary for an even number of  $N_{\text{Tar}}$ , and at least  $2N_{\text{Tar}} - 1$  antenna elements are necessary for an odd number of  $N_{\text{Tar}}$ . In addition, due to the matrix arrangements, at least four receive antennas are required. However, for a spaceborne DBF-SAR, many antenna elements are required, and this limitation is not an issue for the definition of  $\mathbf{Y}[p]$ .

From Equation (5) we can define two overlapping submatrices  $\mathbf{Y}_0[p]$  and  $\mathbf{Y}_1[p]$ , which are shifted by a single element:

$$\mathbf{Y}_0[p] = \begin{bmatrix} u_0[p] & \cdots & u_{L-1}[p] \\ u_1[p] & \cdots & u_L[p] \\ \vdots & \ddots & \vdots \\ u_{N_{\text{Rx}}-L-1}[p] & \cdots & u_{N_{\text{Rx}}-2}[p] \end{bmatrix} \quad \text{and} \quad (8)$$

$$\mathbf{Y}_1[p] = \begin{bmatrix} u_1[p] & \cdots & u_L[p] \\ u_2[p] & \cdots & u_{L+1}[p] \\ \vdots & \ddots & \vdots \\ u_{N_{\text{Rx}}-L}[p] & \cdots & u_{N_{\text{Rx}}-1}[p] \end{bmatrix}. \quad (9)$$

these matrices correspond to the antenna subarrays, which are formed to estimate the linear spatial shift of the impinging signal between both subarrays (cf. Figure 3). Even shifts by more than a single element are possible. The effects have not been studied yet. To find the AoAs, in an intermediate step, we are looking for the estimated values of  $z_m[p]$ , which can be directly obtained by calculation of the generalized eigenvalues  $\Psi$  (e.g., with the standard QR algorithm) of the equation system:

$$\mathbf{Y}_0^\dagger[p] \cdot \mathbf{Y}_1[p] = \left\{ [\mathbf{Y}_0^\dagger[p] \cdot \mathbf{Y}_0[p]]^{-1} \cdot \mathbf{Y}_0^\dagger[p] \right\} \cdot \mathbf{Y}_1[p] = \Psi \cdot \Gamma, \quad (10)$$

where  $\mathbf{Y}_0^\dagger[p]$  denotes the Moore-Penrose pseudo inverse of  $\mathbf{Y}_0[p]$ ,  $*$  is the conjugate transpose, and  $\Gamma$  are the generalized

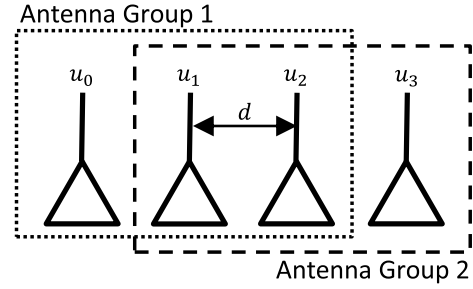


**FIGURE 3** Illustration of the matrix pencil methodology with  $N_{\text{Rx}} = 4$ . In Equation (8) and Equation (9) two submatrices are formed which correspond to the two antenna subarrays *Group 1* and *Group 2*. Via kind of averaging (Equation 10) the linear spatial shift w.r.t. the receive signal and accordingly the AoA is directly calculated

eigenvectors. A more detailed derivation and decomposition of this equation can be found in appendix A. In the following all estimated values are marked with  $\checkmark$ .

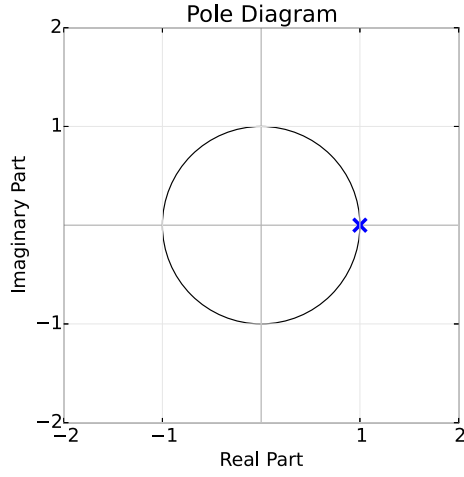
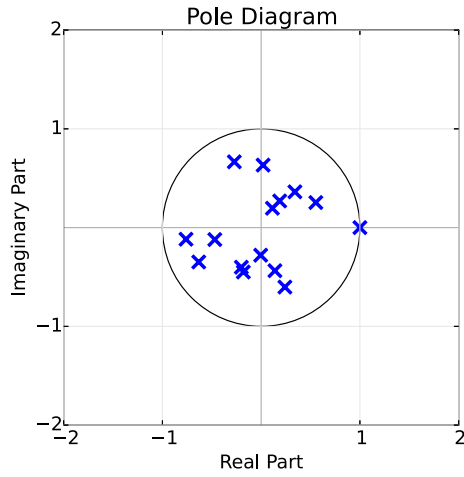
With respect to Equation (4) and Equation (26), it is known that all plausible elements of  $\Psi$  must lie at the unit circle. All remaining values are hence not of interest and can be ignored. However, noise contributions cause a displacement of these eigenvalues from the unit circle. By tolerating a certain margin for this deviation, which is dependent on the signal-to-noise ratio (SNR) of  $\mathbf{Y}[p]$ , an estimate of  $N_{\text{Tar}}$  can be obtained from the data. To give an illustrative example, Figure 4a shows a plot of the pole diagram containing the eigenvalues of  $\Psi$  for  $N_{\text{Tar}} = 1$ ,  $N_{\text{Rx}} = 32$ ,  $L = 1$  and without any additive noise. The single estimated eigenvalue lies exactly at the unit circle and can be treated as a plausible value. In Figure 4b, we can find the pole diagram with the same simulation parameters as before—even without any noise—but with  $L = 15$ . More values than necessary are estimated, while all false estimates are randomly distributed and not lying on the unit circle.

Finally, the demanded angles  $\check{\vartheta}_m[p]$  can be obtained from the imaginary parts of the found eigenvalues through solving Equation (4) for  $\check{\vartheta}_{\text{cm}}$ :

$$\check{\vartheta}_m = \arcsin \left( \frac{\text{Im}\{\ln(\check{z}_m)\}}{\frac{2\pi}{\lambda} \cdot d} \right). \quad (11)$$

Because the generalized eigenvalues of Equation (10) cannot be determined accurately at higher noise levels of the raw data, the variance of the estimated angles will also increase. For an improved accuracy of noisy data and to adapt this preliminary method to the SAR case, some extensions are given in the next subsections.

The forward-backward (FB) averaging approach has also been studied within this investigation. However, we came to the same conclusion as [19, 20]. The averaging helps to improve the accuracy, but the required quadratic shape of the matrix  $\mathbf{Y}$  with  $L = (N_{\text{Rx}} - 1)/2$  leads to too many false estimates. Thus, the FB averaging method is excluded here.

(a)  $L = 1$ .(b)  $L = 15$ .

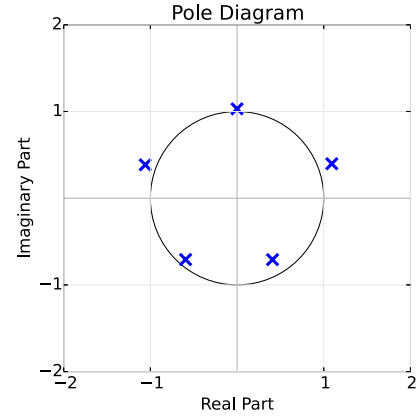
**FIGURE 4** Pole diagrams with the estimated eigenvalues  $\check{z}_m[p]$  of  $\Psi$  using the matrix pencil method for different pencil parameters,  $N_{\text{Tar}} = 1$ ,  $N_{\text{Rx}} = 32$

### 3.3 | Total least squares matrix pencil

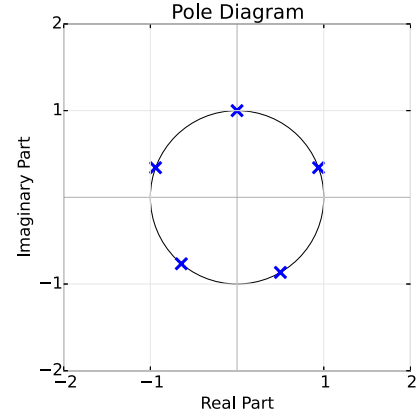
The idea behind the Total Least Squares Matrix Pencil (TLS-MP) makes use of the knowledge that all plausible  $\check{z}_m[p]$  must lie exactly on the unit circle [21]. Eigenvalues, which are perturbed by noise, lie close to the unit circle because the pseudo-inverse of Equation (10) cannot be determined accurately. Via total least squares regression, these poles are *projected* to the unit circle (cf. Figure 5), and more accurate results can be achieved.

The first computation step of the TLS-MP is the Singular Value Decomposition of  $\mathbf{Y}$  from Equation (5):

$$\mathbf{Y} = \mathbf{A} \cdot \mathbf{\Sigma} \cdot \mathbf{B}^H, \quad (12)$$



(a) Generalized eigenvalues perturbed by noise.



(b) Generalized eigenvalues projected on the unit circle by TLS.

**FIGURE 5** Illustration of the total least squares matrix pencil principle with the pole diagram

with  $\mathbf{A}$  and  $\mathbf{B}$  being the left and right singular vectors, respectively.  $\mathbf{\Sigma}$  is a real-valued matrix containing the singular values along the main diagonal and  $^H$  is the Hermitian of the matrix. From theory of matrix computations, it is known that  $\mathbf{Y}$  has  $N_{\text{Tar}}$  non-zero singular values for the noiseless case ( $\mathbf{n} = \mathbf{0}$ ). Otherwise, the raw data matrix  $\mathbf{Y}$  has more singular values, which are not equal to zero. These erroneous singular values and their corresponding singular vectors are not considered in the TLS-MP method. For this, the number of targets  $N_{\text{Tar}}$  must be known beforehand. Otherwise, it is recommended to make use of the threshold value  $\mu$ . This value serves as decision-guidance between plausible and non-plausible singular values of  $\mathbf{Y}$ :

$$\mu \approx 10^{-N_{\text{dig}} \cdot \mu_{\text{max}}}, \quad (13)$$

with  $N_{\text{dig}}$  being the number of significant digits (e.g.  $N_{\text{dig}} = 3$ ) and  $\mu_{\text{max}}$  is the real part of the largest estimated  $\check{z}_m$ :



$$\mu_{\max} = \Re\{\max\{\check{z}_m\}\}. \quad (14)$$

$N_{\text{dig}}$  is an empirical value chosen in dependence on the  $\text{SNR}$  of  $\mathbf{Y}$ . All eigenvalues greater than  $\mu$  correspond to a true target.

Since it is known that all eigenvalues  $\check{z}_m(t)$  with index  $m > N_{\text{Tar}}$  are irrelevant, we can define a filtered version of the Hankel matrix as  $\mathbf{Y}'$ :

$$\mathbf{Y}' = \mathbf{A}' \cdot \mathbf{\Sigma}' \cdot \mathbf{B}'^H. \quad (15)$$

$\mathbf{A}'$ ,  $\mathbf{\Sigma}'$  and  $\mathbf{B}'$  are the submatrices of  $\mathbf{A}$ ,  $\mathbf{\Sigma}$  and  $\mathbf{B}$ , respectively:

$$\begin{aligned} \mathbf{A}' &= \mathbf{A}[:, 1 \dots N_{\text{Tar}}], \\ \mathbf{\Sigma}' &= \mathbf{\Sigma}[1 \dots N_{\text{Tar}}, 1 \dots N_{\text{Tar}}], \\ \mathbf{B}' &= \mathbf{B}[:, 1 \dots N_{\text{Tar}}]. \end{aligned} \quad (16)$$

: denotes that all elements from that row/column are considered.

In analogy to Equation (8) and Equation (9), we form the two submatrices  $\mathbf{Y}'_0$  and  $\mathbf{Y}'_1$  from  $\mathbf{Y}'$ :

$$\begin{aligned} \mathbf{Y}'_0 &= \mathbf{A}' \cdot \mathbf{\Sigma}' \cdot \mathbf{B}'_0^H, \\ \mathbf{Y}'_1 &= \mathbf{A}' \cdot \mathbf{\Sigma}' \cdot \mathbf{B}'_1^H, \end{aligned} \quad (17)$$

where  $\mathbf{B}'_0$  and  $\mathbf{B}'_1$  are equal to  $\mathbf{B}'$  without the last and the first row, respectively.

In the final computation steps of the TLS-MP, we proceed in the same way as for the standard MP. After the calculation of the generalized eigenvalues of the term  $\mathbf{Y}'_0{}^\dagger \cdot \mathbf{Y}'_1$  (cf. Equation 10), the AoA  $\vartheta_m[p]$  can be calculated via Equation (11).

### 3.4 | Modification of the matrix pencil method for extended angular coverage

Up to now, we have proposed methods to improve the accuracy and stability of the basic MP in the presence of noise. This section addresses SAR-inherent signal characteristics, since the point target model of Equation (1) is an idealized point of view and neglects finite pulse durations in combination with extended scatterers. Especially the established condition for narrowband estimation problems does not hold for chirp signals.

From [18], it is known that the received signal at each instant of time is the sum signal of all echoes within the angular pulse extent. Accordingly, the true AoA spans an angular interval, while the MP needs a discrete number for  $N_{\text{Tar}}$ . As a solution, prior known properties of the used transmit signal, and an approximation of the geometrical structure of the scene can be used. According to [22], the variance of the MP estimator can be decreased by using

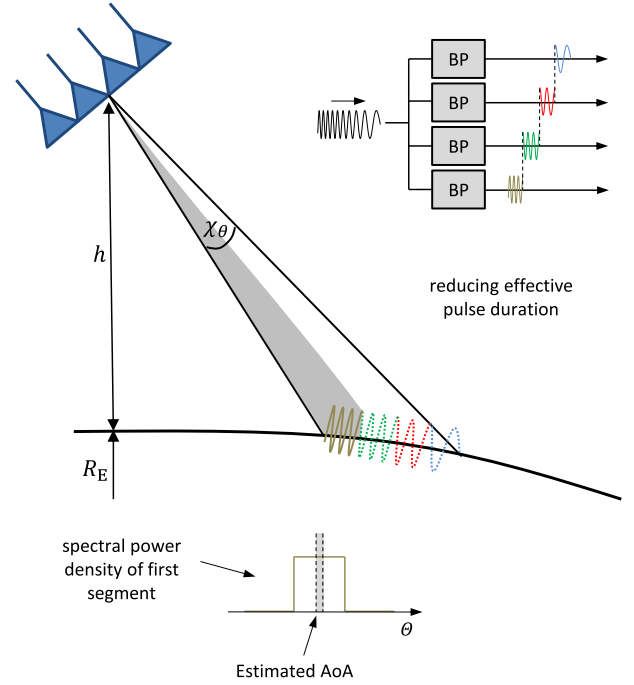


**FIGURE 6** At a certain instant, the echo signal is received from an angular interval. After bandpass filtering, the chirp is synthetically narrowed and accordingly also the angular pulse extent. In dependence on the pencil parameter  $L$  the matrix pencil estimates the mean angle of arrival of this segment, while the grey-coloured bar in the figure indicates the variance

bandpass filters while filtering unwanted noise contributions. In our case, the bandpass brings even more benefits. We propose to implement narrowband bandpass filters in the receive channels to reduce the effective pulse duration of the chirp signal—and hence also the angular pulse extent—while suiting the signal to a narrowband estimation problem.

Under the assumption of homogeneous radar backscatter in the observed scene, the received signal has an equally distributed spatial-spectral power density (cf. Figure 6). Via its inherent averaging (cf. Equation 10), the MP estimates directly—in dependence on the pencil parameter  $L$ —the mean AoA of this bandpass divided pulse echo. At this step, it is very important that the angular interval after bandpass division is smaller than the accuracy limit of the MP. Otherwise, more than a single AoA will be estimated, and the MP bears wrong results. To define the required filter bandwidth, it is necessary to look at the accuracy limit of the MP  $\delta_{\text{MP}}$  and the pulse extent first. Based on the simulation results of Section 4.4, a plausible value for  $\delta_{\text{MP}}$  is approx. 1/10 of the antenna  $\text{HPBW}$  (for required  $\text{SNR}$  values of 10 ... 25 dB). This limit must be greater or equal to the maximum acceptable angular pulse extent  $\chi_\Theta$  after bandpass filtering (cf. Figure 6, [18]). Because  $\chi_\Theta$  varies over  $\Theta$ , we take its maximum (at the near edge of the swath) and calculate the ratio  $\max\{\chi_\Theta(\Theta)\}/\delta_{\text{MP}}$ , which gives the number of angular segments in which the pulse must be divided. The required filter bandwidth is the total signal bandwidth  $B$  divided by the number of segments:

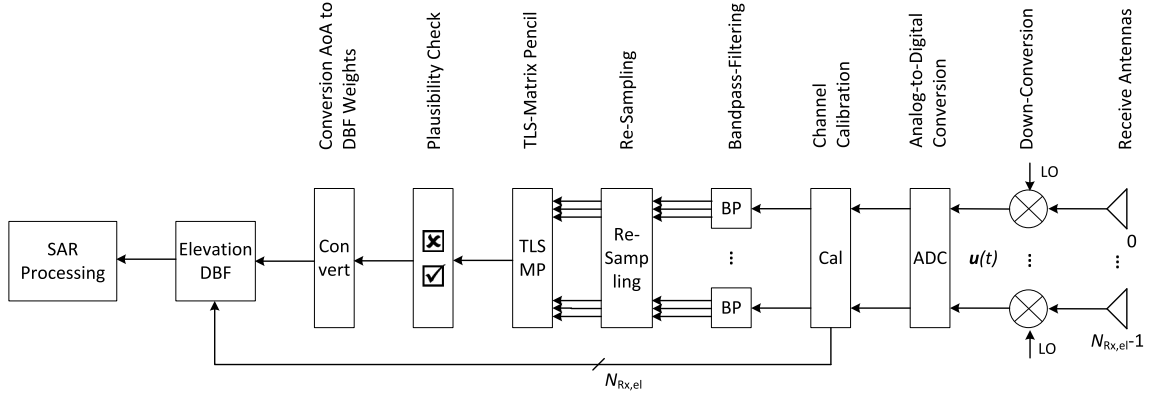


**FIGURE 7** Practical implementation of the matrix pencil method in a DBF-SAR system DBF, digital beam-forming; SAR, Spaceborne synthetic aperture radar

$$B_{BP} = \frac{B \cdot \delta_{MP}}{\max\{\chi_{\Theta}(\Theta)\}}. \quad (18)$$

To give an example, for the values  $\delta_{MP} = 0.05^\circ$ ,  $B = 100$  MHz and  $\max\{\chi_{\Theta}(\Theta)\} = 2.0^\circ$ , we obtain a reasonable filter bandwidth of  $B_{BP} \approx 2.5$  MHz. This results in an effective pulse duration of  $3.0 \mu s$ .

Apart from reducing the angular pulse extent and filtering noise, there is a further benefit of using frequency filters. Insofar as the system complexity and the available amount of computational power for calculating the MP allows, a whole filter bank can be used instead of a single filter. By following this approach, it is possible to estimate the AoA for each spectral part of the whole chirp separately (cf. Figure 6). The set of estimated angles can then be used to obtain information about the Earth's topography more precisely.

### 3.5 | Practical implementation

This section concentrates on the advanced TLS-MP with bandpass filtering, since it is supposed to be the optimum choice for topography-adaptive DBF on receive in SAR.

Figure 7 shows the simplified block diagram of the MP processor. Starting with the receive antennas, the received signals are downconverted to the IF band, digitized with analogue-to-digital converters, and calibrated to compensate for hardware errors and their effects. As suggested in the last section, in each receive channel, a bank of bandpass filters select a narrow frequency band within the chirp bandwidth to reduce the effective pulse duration. A resampling with a lower sampling frequency, tailored to the bandwidth after filtering, lowers the overall computational complexity. In the following block, the TLS-MP algorithm is calculated (for each bandpass filtered signal). Not mentioned yet is the plausibility check, which is placed directly behind the TLS-MP. Since the MP is an estimator and its robustness is completely dependent on the acquired raw data, false estimates can never be excluded. From plausibility considerations, an angular interval can be defined,

from which the echo will be expected. If the estimated angle lies within this interval, it passes the check; otherwise, a theoretical value is used.<sup>2</sup>

If multiple angles are estimated simultaneously (e.g., due to topography), separate buffers for the other AoA are required. The rest of the DBF and image processing must then be designed flexibly to adapt to the appropriate scene.

## 4 | PERFORMANCE ANALYSIS

To gain an insight into the behaviour and accuracy of the MP, a series of simulations have been performed. Some of these results are compared to the Conventional Beam-Former (CBF, Array Factor equivalent) with rectangular windowing, computed via the following equation [23]:

$$\check{\vartheta}_0 = \operatorname{argmax}\{|a^* u|^2\}, \quad (19)$$

while  $\operatorname{argmax}\{\dots\}$  gives the position of the maximum value, which is equal to the estimated AoA.

The following paragraphs show simulation results based on the run time, antenna length, AoA, multiple targets, and spatially extended targets (surfaces). Before showing the results, already some predictions can be noted. According to [6], it is expected that the accuracy of the estimators can be improved by changing the used parameters in the following way:

- Increasing the  $SNR$  of the received echo signal.
- Increasing the physical length  $l$  of the antenna (at keeping the number of antenna elements fixed).
- Increasing the number of antenna elements  $N_{Rx}$  (at keeping the physical length constant).
- Decreasing the angular distance of the AoA from the antenna's broadside direction:  $\min\{|\Theta - \Theta_{tilt}|\}$ .

<sup>2</sup>Alternatively, in substitution of the theoretical value also a mean value of the fore and aft estimated angle along range or a previously estimated angle can be used.

**TABLE 1** Assumed typical parameters of a spaceborne synthetic aperture radar for angle of arrival estimation

Description	Parameter	Value
Transmit peak-power	$P_{Tx}$	3.8 kW
Total radar system losses	$a_{sys}$	4.0 dB
Orbit height	$h$	600 km
Antenna tilt angle w.r.t. nadir	$\theta_{tilt}$	27.25°
Off-nadir steering angle of antenna	$\theta$	15° ... 39.5°
Swath width	$W$	351 km
Signal centre frequency	$f_c$	9.3 GHz
Signal bandwidth	$B$	100 MHz
Pulse duration	$\tau_p$	120 $\mu$ s
Angular pulse extent	$\chi_\Theta$	5.2° ... 1.1°
IF signal sampling frequency	$f_s$	$1.2 \cdot B$ (120 MHz)
Total antenna length in elevation	$l_{el}$	4.2 m
Total antenna length in azimuth	$l_{az}$	8.0 m
No. of receive antenna elements In elevation	$N_{el}$	54
No. of receive antenna elements In azimuth	$N_{az}$	8
Receive antenna element separation In azimuth	$d_{az}$	1.0 m
Receive antenna element separation In elevation	$d_{el}$	7.7 cm
Mean <i>HPBW</i> after DBF	$HPBW_{DBF}$	0.44°

Abbreviations: DBF, digital beam-forming; HPBW, half-power beamwidth.

- Increasing the number of independent snapshots  $N_{sn}$  (i.e. increasing the sample size for averaging).

These predictions result from derivations made via the Cramer–Rao lower bound (CRLB) in the appendix of [6]. To have a common basis for all simulations, a realistic spaceborne DBF-SAR with the system parameters listed in Table 1 serves as a reference for all simulations. The element spacing of greater than  $\lambda/2$  is chosen to reduce the number of elements by keeping the antenna size constant for the *HPBW*. Since the resulting grating lobes lie outside the swath, they can be considered implausible and neglected for signal processing. Due to the still relatively large number of receive antenna elements in elevation ( $N_{Rx, el} = 54$ ), it must be noted that not all channels must be digital but can be grouped in subapertures with a combination of analogue and DBF. For the bank of bandpass filters (cf. Equation 18), a filter bandwidth of  $B_{BP} = 2.5$  MHz was used. Regarding the practical realization, the output signal of each filter has also been resampled to the lower sampling frequency of  $f_s = 1.2 \cdot B_{BP} = 3.0$  MHz. In azimuth, fewer antenna elements are required, since usually in

this direction, DBF is used only to reconstruct a wider Doppler spectrum [3]. Because we concentrate solely on the elevation direction, the number of azimuth antenna elements does not yet play a role. The azimuth extension is required for the investigation of Section 4.4.

#### 4.1 | Evaluation of the computational complexity

Usually, the computational complexity of an algorithm is expressed using the big O notation  $\mathcal{O}$  [24]. It describes the asymptotic behaviour of the algorithm's run time if the arguments tend to a certain value. This has the significant advantage that the comparison is fair and independent of the implementation (programming style and language), operating system, and computer. Unfortunately, a straightforward comparison between the estimation algorithms is still difficult since the covariance matrix for spectral MUSIC, Root MUSIC, and LS-ESPRIT is computed for the whole acquired echo window (full swath) at once. Thus, to make this comparison more realistic, the swath is divided into a total number of 100 sub-swath cells. Then the algorithms are repeatedly applied to finally cover the full swath. A closed-form derivation of the complexities would be beyond the scope of the paper because they are composed of a complex construct of different individual calculations, like eigenvalue decompositions, correlation matrices, covariance matrices, ... Thus, the interested reader is referred to the appendix of [25].

The two most driving parameters of the complexity are the signal bandwidth and the number of antenna elements. Using the radar system parameters listed in Table 1, the run times for the individual algorithms versus  $B$  and  $N_{el}$  are plotted in Figure 8. The dependence on the signal bandwidth  $B$ , which is related to the sampling frequency by  $f_s = 1.2 \cdot B$ , leads to a change in the number of acquired samples per echo window and has been considered.

It becomes apparent that the run time of spectral MUSIC is always the highest and about  $10^4$ – $10^6$  times higher than for the MP. In addition, Root MUSIC and LS-ESPRIT need a fairly large number of iterations. Especially changes of the signal bandwidth show a greater impact than for the MP-based algorithms. This can be justified by the expensive computation of a large correlation matrix in those methods. In the end, the MP and TLS-MP have quite similar computational complexity and outperform the covariance methods by far.

A system as described in Table 1 has an echo signal duration of 10 ms. To guarantee a real-time capability, the complete calculation of the  $2.15 \cdot 10^{10}$  TLS-MP tasks must be finished within one echo window of less than 10 ms. If a state-of-the-art space-qualified FPGA shall be used, a DSP computing performance of more than 8 TeraMACs and a speed of 850 MHz is available (e.g. XILINX Kintex UltraScale XCKU085). It is known that the computational complexity via  $\mathcal{O}$  and MACs cannot be directly compared, so they shall lead to only a rough order of magnitude for our proof. Taking into



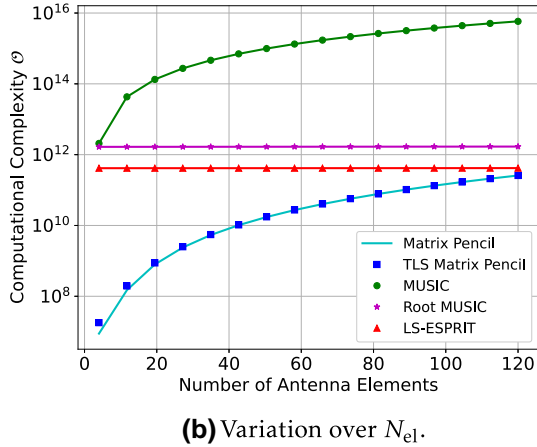
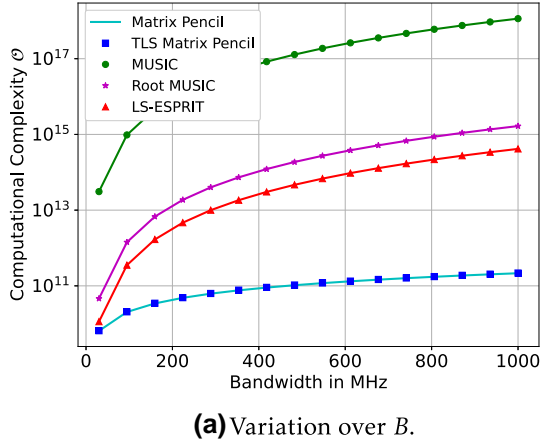


**FIGURE 8** Computational complexity of common estimation algorithms ESPRIT, estimation of signal parameters using rotational invariance techniques; TLS, total least squares

account that the capacity of the FPGA allows also for parallelization of the 40 bandpass filtered signals, and of at least 100 range samples in parallel, the calculation is finished within  $(2.15 \cdot 10^{10} / (40 \cdot 100)) / 850 \cdot 10^6 \text{ 1/s} = 6.3 \text{ ms}$ . Apart from the fact that a more optimized implementation and the FPGA's capacity allow for even more parallelized tasks, the processing time is already shorter than the maximum duration of an echo window. A real-time implementation can hence be guaranteed. With respect to the block diagram of Figure 7 all main processing tasks up to elevation DBF can be computed on a single FPGA. While MUSIC and ESPRIT are in a completely different order of computational complexity, even with high-performance FPGAs they cannot be processed in time.

## 4.2 | Angular estimation of a single point target

All simulations of this section serve to study the MP method's fundamental behaviour and performance via individual point targets. In a self-developed Python routine, a full DBF-radar simulation setup including the transmitted chirp signal, noise, and a realistic geometrical spaceborne model, has been

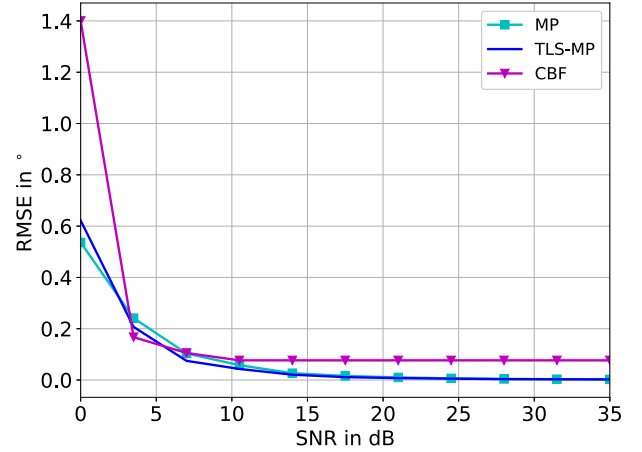


**FIGURE 9** Root mean square error of the estimated angle with respect to the expectation value over varying signal-to-noise ratios. MP: matrix pencil ( $L = 2$ ), TLS-MP: total least squares matrix pencil ( $L = 2$ ), CBF: conventional beam-former with rectangular windowing

implemented for this task. It is known that MUSIC and ESPRIT can be applied only on narrowband signals. With respect to  $B = 100 \text{ MHz}$ , truly a broadband signal is used, and further adapted preprocessing steps are required (e.g. range-compression). Because this would lead to a deceptive comparison, we decided to omit this analysis.

**Varying SNR:** It is expected, that for higher SNR, the AoA can be estimated more accurately. The simulation result, given in this paragraph, should prove this prediction and show the accuracy in comparison to the CBF with rectangular windowing. For the simulations, a point target was located at  $\theta = +1.5^\circ$  from antenna broadside direction ( $\Theta = 28.75^\circ$ ) and its specific target scattering coefficient was varied at a constant noise level to realize a SNR-range from 0.0 to 35.0 dB. Figure 9 shows the Root-Mean-Square Error (RMSE) of the estimated angle with respect to the expectation value  $E[\dots]$ :

$$\text{RMSE}(\check{\theta}) = \sqrt{E[\check{\theta} - \theta]} = \sqrt{\text{bias}^2(\check{\theta}) + \text{var}(\check{\theta})}. \quad (20)$$

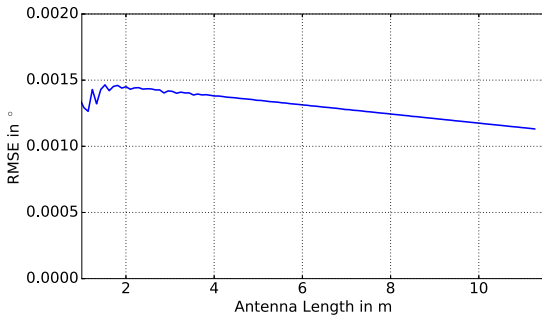
The result was obtained after a Monte Carlo simulation with a total number of 100 independent trials. In general, it can be observed that the variance decreases with increasing SNR, which stands in direct agreement with the results of the CRLB in [6]. A further general observation is that all three methods for SNR values  $> 12 \text{ dB}$  display a weak dependence of the RMSE and that the CBF has a higher error. This result also stands fully in agreement with the observations made in [26].

**Length of the Full Antenna Array:** In this consideration, due to the relatively high bias of the CBF method in Figure 9, the result was omitted to show the trend of the MP more precisely. In this section, the dependence of the variance solely on different electrical antenna lengths  $l$  is analysed. This analysis is carried out, therefore, in the absence of noise and no additional averaging techniques are applied. To change the full

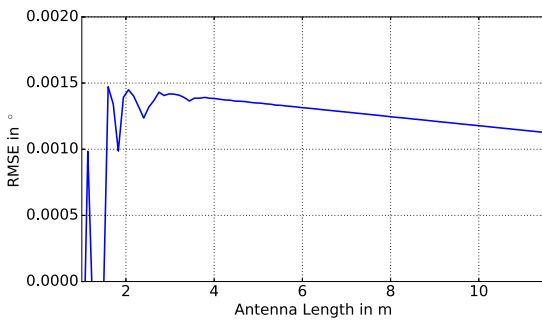
antenna length, it is either possible to vary the number of elements or to vary the element separation. Both cases are treated next.

A direct comparison between Figure 10a and Figure 10b shows that after a minimum electrical antenna length of approximately 3.0 m, the results are equal regardless of whether  $N_{\text{Rx}}$  or  $d$  is varied. Because the *HPBW* of a smaller antenna would be greater than  $1.3^\circ$ , which is not suitable for our DBF concepts, this limit can be accepted. The bias of less than  $0.0015^\circ$ , which decreases with increasing antenna length, is negligible for SAR applications. The observed bias value is not an effect of the *SNR*, since there was no noise added in this simulation. In view of the observations noted in the next paragraph, an explanation lies in the angular position of the target at  $\theta = 28.75^\circ$ , which brings a systematic error with respect to the antenna steering angle. If the target were exactly at antenna broadside direction ( $\theta = 27.25^\circ$ ), there would be no dependence on the antenna aperture size or number of elements.

The authors do not want to hide that implausible results may generally occur and lead to a NaN if the matrix cannot be solved. Especially in Figure 10b at an antenna length of approx. 1.0 m this can be observed.



**(a)** Antenna length varied over a fixed element spacing of  $d = 2.4\lambda$ ,  $N_{\text{Rx}} = 4 \dots 150$ .



**(b)** Antenna length varied over a fixed number of elements:  $N_{\text{Rx}} = 54$ ,  $l_{\text{ant,el}} = 0.1 \text{ m} \dots 10.2 \text{ m}$ .

**FIGURE 10** Root mean square error of the estimated angle with respect to the expected value over varying antenna length

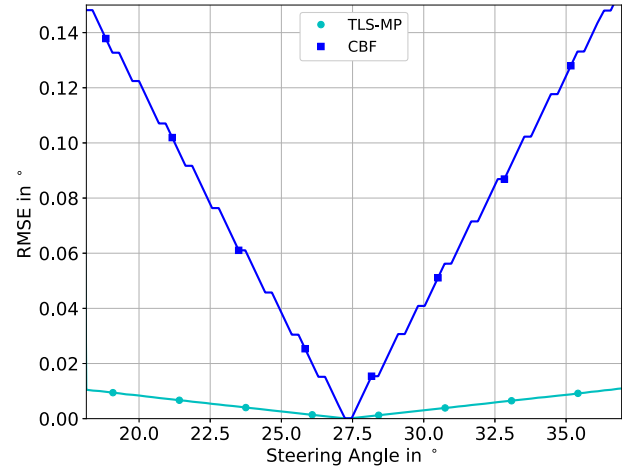


**FIGURE 11** Root mean square error of the estimated angle with respect to the expectation value over varying steering angle

**Varying Steering Angle:** The CRLB predicts that the accuracy of the estimated angle decreases with increasing AoA from antenna broadside direction. The simulation shows in Figure 11 that the bias rises linearly up to  $0.01^\circ$  at the edges of the swath. Because this deviation leads to a noticeable contribution with respect to our maximum tolerable accuracy of  $\delta_{\text{MP}} = 0.05^\circ$ , this effect must be accounted for.

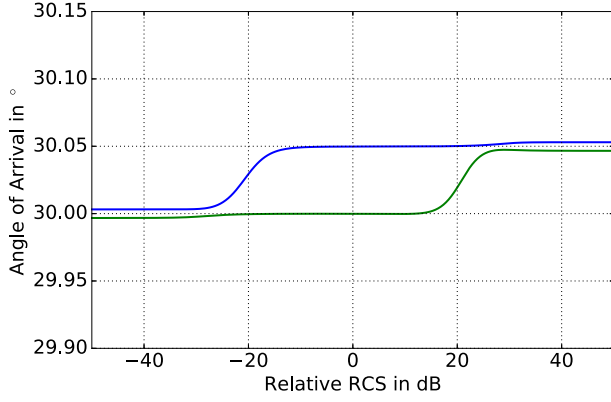
For comparison also the result of the CBF is shown. As expected, the deviation is approx. 10 times larger than for the TLS-MP, and there is a significant influence of the grating lobes noticeable.

### 4.3 | Multiple individual targets

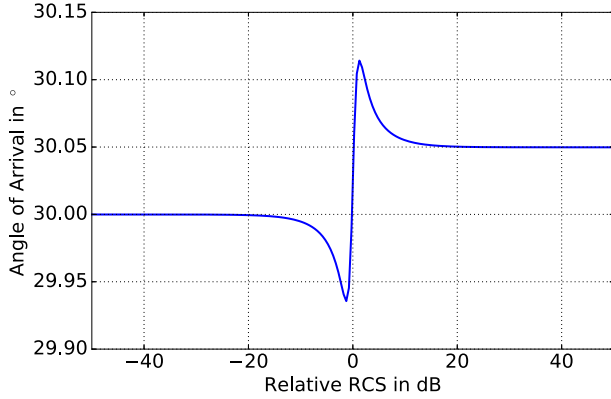
In the scenario considered here, two point targets at  $\theta_1 = 30.0^\circ$  and  $\theta_2 = 30.05^\circ$  have been simulated. While the first target has a constant radar cross-section (RCS), the RCS of the second target was varied with respect to the first one in the range  $-50 \text{ dB} \dots 50 \text{ dB}$ . Noise perturbation was neglected.

The plot in Figure 12a shows the estimated AoAs with the two largest eigenvalues of Equation (10),  $L = N_{\text{Tar}} = 2$ . One can see that the targets with an angular separation of just  $0.05^\circ$  can be sufficiently resolved if the relative difference between the two RCS is less than  $\pm 20 \text{ dB}$ . We note, for instance, within an RCS range of  $[20 \text{ dB}, 50 \text{ dB}]$ , no information about the AoA can be given, since the low RCS of the second target is completely dominated by the first. Outside the bounds of  $[-30 \text{ dB}, 30 \text{ dB}]$ , the second target response appears as noise and both estimated angles correspond to the strongest target. However, there is mutual interaction between the two targets and the expectation values could not be exactly reached with a negligible bias of  $\pm 0.003^\circ$ .

In another case, also two point targets have been simulated. But the TLS-MP was calculated on purpose with the wrong assumption  $L = 2$ ,  $N_{\text{Tar}} = 1$ . The result in Figure 12b shows a step at a relative RCS of  $0.0 \text{ dB}$  and that the angle of one of the two targets could be estimated without any bias.



(a) TLS-MP with  $N_{\text{Tar}} = 2$ .



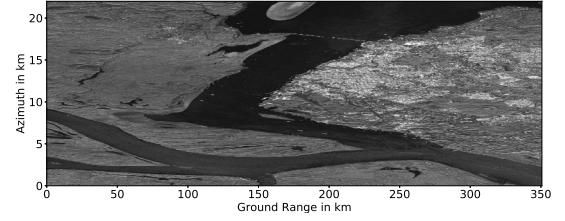
(b) TLS-MP with  $N_{\text{Tar}} = 1$ .

**FIGURE 12** Estimated angle for two simulated point targets at  $\theta_1 = 30.0^\circ$  and  $\theta_2 = 30.05^\circ$  with varying relative radar cross sections

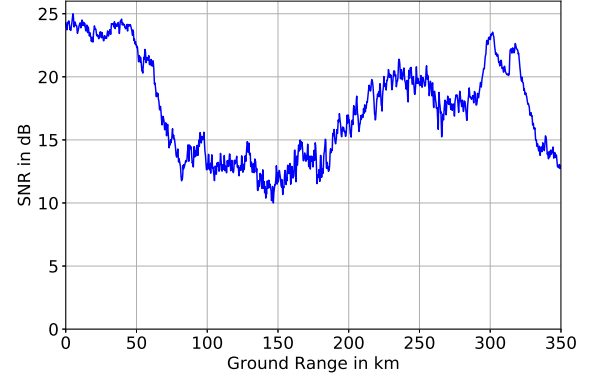
#### 4.4 | Targets with spatial extension

Up to now, only basic angular estimation tasks with discrete point targets have been considered. This is beneficial to get an impression of which way the MP behaves in different cases. Since spaceborne SAR is inherently used for imaging of large distributed scatterers, for example forests or crops, a simulation is necessary, which proves the suitability of the MP method for such areas of operation. Especially the influence of numerous scatterers with random individual phases distributed over the antenna footprint in azimuth and elevation shall be analysed via this simulation.

Our self-developed simulation tool takes the geometrical and radar parameters of Table 1 to simulate a realistic radar receive signal. By using an original SAR image, acquired with the radar satellite TerraSAR-X [27], we implemented a scattering model. The original scene (cf. Figure 13) has been taken, reshaped to the maximum scanning angle along elevation ( $\theta = 15^\circ \dots 39.5^\circ$ ) and a quasi-azimuth extension of 22.0 km. The radar receive signal at the receive antenna elements is generated by summing up all chirp signal echoes within the



(a) Original SAR scene of Manaus acquired with TerraSAR-X.



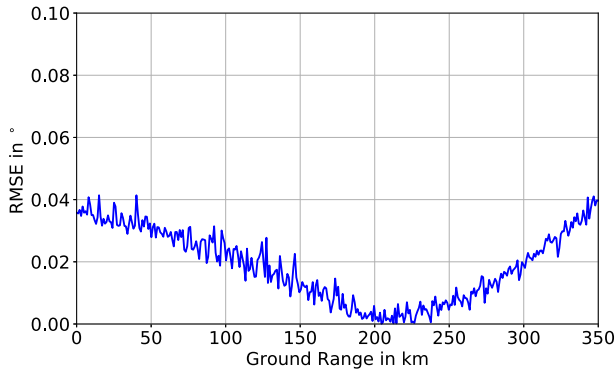
(b) Extracted range profile.

**FIGURE 13** Original synthetic aperture radar scene and extracted range profile

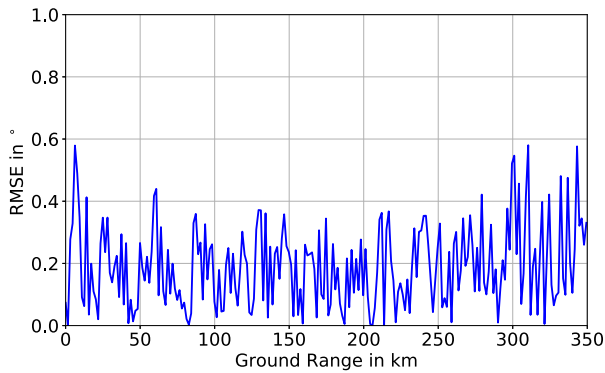
footprint. Basically, individual chirp signals are shot and reflected at 10 point targets per resolution cell to emulate a distributed scattering scenario. By adding noise, the amplitude of the receive signal was scaled to a dynamic SNR variation of 10 ... 25 dB. Finally, this approach generates a quasi-realistic radar receive signal from a large number of individual distributed scatterers. Figure 13b shows the equivalent range profile of the receive signal's SNR for this scene.

Following the processing scheme, which was suggested in Section 3.5, the TLS-MP with bandpass filtering was applied on the simulated radar raw data. In Figure 14a we can see the corresponding plot showing the RMSE of the estimated angle versus the true AoA. While the trend itself is very similar to that shown in Figure 11, the absolute amount of deviation is more significant in this case. Obviously, the main contribution to the angular deviation results from antenna steering and not from variation in the RCS. Initially we accept this result because it fully applies to our requirements. In further studies we will analyse distributed scattering scenarios—and especially the influence of the bandpass filters—in more detail.

We also applied the CBF method on the same data with bandpass division of the received signal for comparison. Due to  $d_{\text{el}} \gg \lambda/2$ , ambiguities resulting from grating lobes have been ignored via plausibility reasons because they lie outside



(a) Matrix Pencil Method.



(b) Conventional Beam-Former.

**FIGURE 14** Root mean square error of the estimated angle with respect to the expectation value for a realistic synthetic aperture radar scene

the swath. A key result of this analysis can be found in Figure 14b. It seems that the RMSE is in the order of the antenna *HPBW* in elevation. This proves basically that CBF can also be applied for this task; however, it provides only low and insufficient accuracy for our purpose.

## 5 | CONCLUSION

While the most accurate and public available global DEM is the one of the TanDEM-X mission with a 90 m grid and a <10 m height accuracy, its memory size is 0.5 TByte [28]. In terms of accuracy, this may be sufficient. However, the data may not be up to date, and there is a dependency on the source. Thus, this study aims to find an effective and highly accurate method to correct for antenna mispointing in the presence of topography for future spaceborne DBF-SAR and MIMO-SAR. It has been found that the MP serves as a proper candidate for this ambition. Apart from a basic derivation of the MP method, additional improvements and adaptations to SAR and possible practical implementation are described. A series of promising simulation results shows the capabilities and key benefits of the MP for topography-adaptive DBF in future SAR.

It was previously known that the accuracy of the MP improves for higher *SNR*, larger antenna lengths, or averaging over independent snapshots. This paper completely confirms these predictions and gives, in addition, an impression about the quantitative sensitivity of the MP method. We also found that after reaching a certain threshold limit of all the analysed parameters, the required accuracy is reached, and there is no need for additional requirements on the typical DBF-SAR sensor. However, it must be taken into account that averaging over several snapshots in azimuth direction and the described bandpass filtering approach are crucial implementations.

The MP can even be applied in scenarios where the other algorithms completely fail to work (e.g. extended targets). This is because most of the other estimators have been derived for discrete AoA detection in communications with non-uniform spatial PSD distributions. While the advanced version of the MP with a combination of TLS and bandpass filtering is highly related to the DBF-SAR signal model, the FB MP finds no application. However, one of the major advantages of the MP is the very fast computation without the need for a correlation matrix. This satisfies the implementation in real-time on-board of a satellite to enable topography-adaptive DBF.

This first paper about the MP method in DBF-SAR serves as the fundamental basis for further studies in this field. In future work, it is planned to run further simulations and improvements on the MP method. In addition, we plan a practical verification via measurement results of a true SAR scene with the new airborne DBF-SAR sensor of the German Aerospace Centre with 12 digital receive channels in X-band [29].

## ORCID

Tobias Rommel  <https://orcid.org/0000-0003-1864-7585>

Sigurd Huber  <https://orcid.org/0000-0001-7097-5127>

Marwan Younis  <https://orcid.org/0000-0002-8563-7371>

## REFERENCES

1. Suess, M., Wiesbeck, W.: Side looking SAR system, United States Patent 6870500, (2005)
2. Kim, J.H.: Multiple-input multiple-output synthetic aperture radar for multimodal operation, (Dissertation), Karlsruhe Institute of Technology (KIT), (2011)
3. Krieger, G., Gebert, N., Moreira, A.: Unambiguous SAR signal reconstruction from nonuniform displaced phase centre sampling, *IEEE Geosci. Remote Sensing Lett.* 1, (4), 260–264 (2004)
4. Bordoni, F., et al.: Adaptive scan-on-receive based on spatial spectral estimation for high-resolution, wide-swath synthetic aperture radar. In: *IEEE International Geoscience and Remote Sensing Symposium*, vol. 1, pp. I–64–I–67 (2009)
5. Balanis, C.A.: *Antenna theory: analysis and design*, 3rd ed. John Wiley & Sons, New Jersey (2005). ISBN: 978-0471667827
6. Stoica, P., Moses, R.: *Introduction to spectral analysis*. Prentice-Hall, New Jersey (1997). ISBN: 978-0132584197
7. Schmidt, R.O.: A signal subspace approach to multiple emitter location and spectral estimation. Dissertation, Stanford University, Stanford (1981)
8. Barabell, A.: Improving the resolution performance of eigenstructure-based direction-finding algorithms. In: *IEEE International Conference*

- on Acoustics, Speech, and Signal Processing, vol. 8, pp. 336–339. IEEE, New York (1983)
9. Roy, R., Kailath, T.: ESPRIT-estimation of signal parameters via rotational invariance techniques. *IEEE Trans. Acoust., Speech, Signal Processing*. 37(7), pp. 984–995 (1989)
  10. Peters, G., Wilkinson, J.H.:  $Ax = \lambda Bx$  and the generalized eigenproblem. *SIAM J. Numer. Anal.* 7(4), 479–492 (1970)
  11. Ikramov, K.D.: Matrix pencils: theory, applications, and numerical methods. *J. Math. Sci.* 64(2), 783–853 (1993)
  12. Ouibrahim, H., Weiner, D.D., Sarkar, T.K.: A generalized approach to direction finding. In: MILCOM 1986. IEEE Military Communications Conference—Communications-Computers: Teamed for the 90's, 1986. vol. 3, pp. 41.4.1–41.4.5. IEEE, New York (1986)
  13. Hua, Y., Sarkar, T.K.: Matrix pencil method for estimating parameters of exponentially damped/undamped sinusoids in noise. *IEEE Trans. Acoust. Speech. Signal Process.* 38(5), 814–824 (1990)
  14. Ozsoy, S., Ergin, A.A.: Pencil back-projection method for SAR imaging. *IEEE Trans. Image Process.* 18(3), 573–581 (2009)
  15. Suess, M., Wiesbeck, W.: Side-looking synthetic aperture radar system, European Patent EP 1 241 487, (2002)
  16. Bordoni, F., et al.: The effect of topography on SCORE: an investigation based on simulated spaceborne multichannel SAR data. In: EUSAR 12th European Conference on Synthetic Aperture Radar. pp. 1130–1134. VDE Verlag, Berlin (2018)
  17. Younis, M., et al.: Performance comparison of reflector- and planar-antenna based digital beam-forming SAR, *Int. J. Antenn. Propag.* 2009, 1–13 (2009)
  18. Younis, M., et al.: On the pulse extension loss in digital beamforming SAR. *IEEE Geosci. Remote Sensing Lett.* 12(7), 1436–1440 (2015)
  19. Pillai, S.U., Burrus, C.S.: Array signal processing. Springer-Verlag, Berlin (1989). ISBN: 978-1461281863
  20. Le Marshall, N.W.D., Tirkel, Z.A.: Modified matrix pencil algorithm for terminite detection with high resolution radar. *Prog. Electromagn. Res. C.* 16, 51–67 (2010)
  21. Adve, R.S.: Elimination of the effects of mutual coupling in adaptive thin wire antennas. Dissertation, Syracuse University, New York (1996)
  22. Hu, F., Sarkar, T.K., Hua, Y.: Utilization of bandpass filtering for the matrix pencil method. *Sig. Process. IEEE Trans.* 1993, 41(1), (1993)
  23. Veen, V.B.D., Buckley, K.M.: Beamforming: a versatile approach to spatial filtering. *IEEE ASSP Mag.* 5, (2), 4–24 (1988)
  24. Dahmen, W., Reusken, A.: *Numerik für Ingenieure und Naturwissenschaftler*. Springer-Verlag, Berlin (2008). ISBN: 978-3540764922
  25. Rommel, T.: Development, implementation, and analysis of a multiple-input multiple-output concept for spaceborne high-resolution wide-swath synthetic aperture radar. Dissertation, Technical University Chemnitz, Chemnitz (2018)
  26. Rio, J.E.F., Sarkar, T.K.: Comparison between the matrix pencil method and the fourier transform technique for high-resolution spectral estimation. *Digit. Signal Process.* 6(2), 108–125 (1996)
  27. Werninghaus, R., Buckreuss, S.: The TerraSAR-X mission and system design. *IEEE Trans. Geosci. Rem. Sens.* 48(2), 606–614 (2010)
  28. Guide, E.G.D.: (2021). <https://geoservice.dlr.de/web/dataguide/tdm90/>, Website, 20.04.2021
  29. Reigber, A., et al.: First interferometric trials with the airborne digital-beamforming DBFSAR system. In: 12th European Conference on Synthetic Aperture Radar EUSAR 2018. pp. 1–4. VDE Verlag, Berlin (2018)

**How to cite this article:** Rommel T, Huber S, Younis M, Chandra M. Matrix pencil method for topography-adaptive digital beam-forming in synthetic aperture radar. *IET Radar Sonar Navig.* 2021;1–14. <https://doi.org/10.1049/rsn2.12103>

## APPENDICES

### Mathematical solution of the matrix pencil

This appendix mathematically describes the solution of the equation system in Equation (10).

After singular value decomposition of Equation (8) and Equation (9) we get respectively:

$$Y_0 = \Lambda \cdot \Xi \cdot V \quad (21)$$

and

$$Y_1 = \Lambda \cdot \Xi \cdot \Psi \cdot V \quad (22)$$

with

$$\Lambda = \begin{bmatrix} 1 & 1 & \dots & 1 \\ z_0 & z_1 & \dots & z_{N_{\text{Tar}}-1} \\ \vdots & \vdots & \ddots & \vdots \\ z_0^{N_{\text{Rx}}-L-1} & z_1^{N_{\text{Rx}}-L-1} & \dots & z_{N_{\text{Tar}}-1}^{N_{\text{Rx}}-L-1} \end{bmatrix}, \quad (23)$$

$$\Xi = \begin{bmatrix} A_0 & 0 & \dots & 0 \\ 0 & A_1 & \dots & 0 \\ \vdots & \vdots & \ddots & \vdots \\ 0 & 0 & \dots & A_{N_{\text{Tar}}-1} \end{bmatrix}, \quad (24)$$

$$V = \begin{bmatrix} 1 & z_0 & \dots & z_0^{L-1} \\ 1 & z_1 & \dots & z_1^{L-1} \\ \vdots & \vdots & \ddots & \vdots \\ 1 & z_{N_{\text{Tar}}-1} & \dots & z_{N_{\text{Tar}}-1}^{L-1} \end{bmatrix} \quad (25)$$

and

$$\Psi = \begin{bmatrix} z_0 & 0 & \dots & 0 \\ 0 & z_1 & \dots & 0 \\ \vdots & \vdots & \ddots & \vdots \\ 0 & 0 & \dots & z_{N_{\text{Tar}}-1} \end{bmatrix}. \quad (26)$$

The matrix pencil:

$$Y_1 - \eta \cdot Y_0 = \Lambda \cdot \Xi \cdot (\Psi - \eta \cdot I) \cdot V \quad (27)$$



has the rank  $N_{\text{Tar}}$  if  $N_{\text{Tar}} \leq L \leq N_{\text{Rx}} - N_{\text{Tar}}$ , while this rank can be reduced to  $N_{\text{Tar}} - 1$ , if  $\eta = z_m$ . Noting that  $\mathbf{I}$  is the identity matrix. Therefore,  $z_m$  can be denoted as the generalized eigenvalues of  $\{\mathbf{Y}_1, \mathbf{Y}_0\}$ . Accordingly, it is also valid to write

$$\mathbf{Y}_1 \cdot \boldsymbol{\Gamma}_m = z_m \cdot \mathbf{Y}_0 \cdot \boldsymbol{\Gamma}_m, \quad (28)$$

where  $\boldsymbol{\Gamma}_m$  denotes the generalized eigenvector corresponding to  $z_m$ . Equation (28) can be rearranged to the form

$$\left( \mathbf{Y}_0^\dagger \cdot \mathbf{Y}_1 - z_m \cdot \mathbf{I} \right) \cdot \boldsymbol{\Gamma}_m = \mathbf{0}, \quad (29)$$

which shows that the values for  $z_m$  can be obtained by calculating the eigenvalues of  $\mathbf{Y}_0^\dagger \cdot \mathbf{Y}_1$ . Noting that  $^\dagger$  represents the Moore-Penrose pseudo inverse.

### Estimation of the signal-to-noise ratio on receive

From chapter IV we know that the MP method requires at least 10 dB SNR of the radar receive signal. In the following we prove that in a true spaceborne scenario this limit can be achieved. We note that the MP uses the signal of a single pulse echo and the radar equation in its basic form can be applied for this estimation.

In a first step we make use of the parameters listed in Table 1. To calculate the area on ground associated with the pulse echo  $A_{\text{foot}}$  the angular pulse extent in elevation is required. With respect to [18] for  $\tau_p = 3.0 \mu\text{s}$  the angular pulse extent is  $0.07^\circ$  (effective pulse duration after bandpass division). The azimuthal width of the antenna footprint can be calculated via the *HPBW* for the single-element aperture  $l_{\text{az}} = 8.0/8 \text{ m}$  and leads to a width of 22 km at the swath centre. This results to  $A_{\text{foot}} \approx 12 \text{ km}^2$ .

While for transmission a single elevation row of the full antenna aperture is used on receive, we can take benefit of the DBF technique and use the full available aperture. Thus, the transmit and receive antenna gains are  $G_{\text{Tx}} = 38.7 \text{ dBi}$  and  $G_{\text{Rx}} = 56 \text{ dBi}$ , respectively. The expected receive power can be calculated via the radar equation:

$$P_{\text{Rx}} = P_{\text{Tx}} \cdot \frac{G_{\text{Tx}} \cdot G_{\text{Rx}} \cdot \lambda^2 \cdot \sigma_0 \cdot A_{\text{foot}}}{(4\pi)^3 \cdot R^4 \cdot a_{\text{sys}}}, \quad (30)$$

while  $\sigma_0$  denotes the differential scattering coefficient and  $R$  is the slant range radar—target at the swath centre. With a mean  $\sigma_0$  of  $-10 \text{ dB}$  and  $R = 675 \text{ km}$ , we obtain  $P_{\text{Rx}} = -79 \text{ dBm}$ .

Finally, by considering the Johnson–Nyquist noise power  $P_{\text{noise}} = k_B \cdot T_0 \cdot B \cdot a_{\text{sys}}$ , the SNR is 11.4 dB. Accordingly, the requirement is fulfilled for the assumed case.